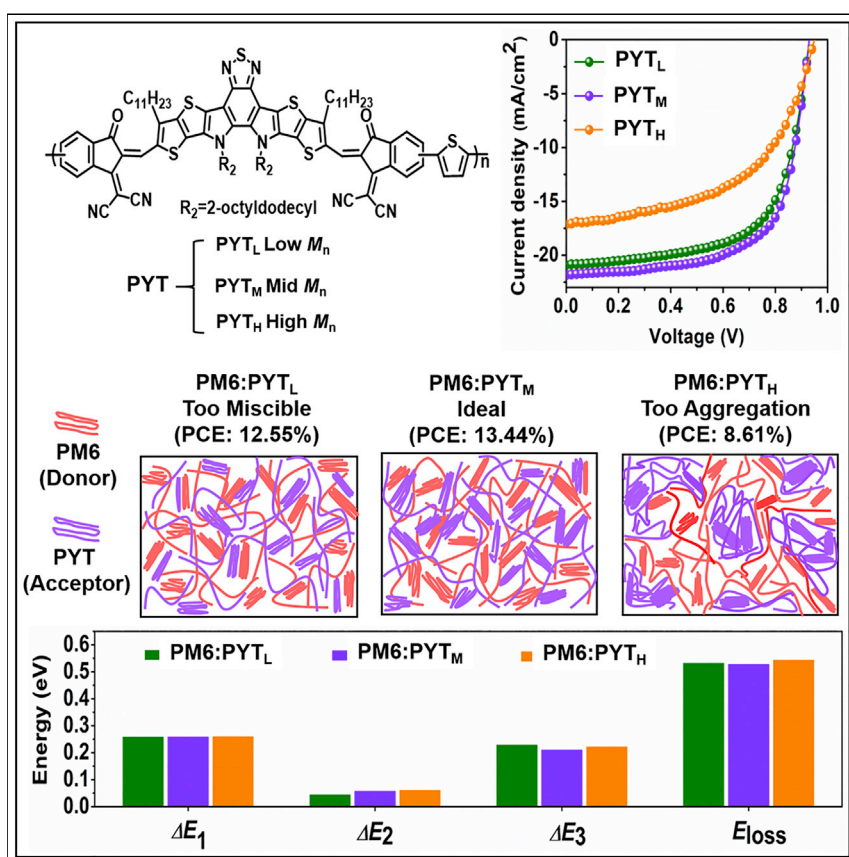


Article

Controlling Molecular Mass of Low-Band-Gap Polymer Acceptors for High-Performance All-Polymer Solar Cells



A narrow-band-gap polymer acceptor (P_A), namely PYT, is reported, while a series of PYT polymer acceptors with controlled average molecular weight (M_n) values were synthesized for fine-tuning the molecular crystallinity and miscibility. When fabricated into all-PSCs with a polymer donor (P_D) PM6, we observed a clear M_n dependence on device performance. The PM6:PYT_M device gives a record-high PCE of 13.44% for the all-PSCs, resulting from the good P_D - P_A pair miscibility, suitable blend microstructure, and improved charge transport properties.

Wei Wang, Qiang Wu, Rui Sun, ..., Wenyan Yang, Hongneng Li, Jie Min

min.jie@whu.edu.cn

HIGHLIGHTS

A fused-aromatic-ring-constructed polymer acceptor is reported

Donor-acceptor miscibility can be modified by optimizing molecular mass

A PYT_M-based all-PSC exhibits an excellent PCE of 13.44%

The molecular weight of polymers plays a vital factor for high-performance all-PSCs

Wang et al., Joule 4, 1070–1086

May 20, 2020 © 2020 Elsevier Inc.

<https://doi.org/10.1016/j.joule.2020.03.019>



Article

Controlling Molecular Mass of Low-Band-Gap Polymer Acceptors for High-Performance All-Polymer Solar Cells

Wei Wang,^{1,4} Qiang Wu,^{1,4} Rui Sun,¹ Jing Guo,¹ Yao Wu,¹ Mumin Shi,¹ Wenyan Yang,¹ Hongneng Li,¹ and Jie Min^{1,2,3,5,*}

SUMMARY

Recent advances in the development of polymer acceptors and the investigation of molecular mass have boosted the power conversion efficiency (PCE) of all-polymer solar cells (all-PSCs) to approximately 11%. Here, a fused-aromatic-ring-constructed polymer acceptor PYT (Poly[(2,2'-((2Z,2'Z)-((12,13-bis(2-octyldodecyl)-3,9-diundecyl-12,13-dihydro[1,2,5]thiadiazolo[3,4e]thieno[2'',3'':4',5']thieno[2',3':4,5]pyrrolo[3,2-g]thieno[2',3':4,5]thieno[3,2-b]-indole-2,10-diyl)bis(methanylylidene))bis(3-oxo-2,3-dihydro-1H-indene-2,1-diylidene)) dimalononitrile-alt-2,5-thiophene)]) is reported, while a series of PYT polymers with different molecular masses (designated as PYT_L, PYT_M, and PYT_H) are prepared to fine-tune the molecular crystallinity and miscibility. Benefiting from the advantages of PYT series, which possess broad absorption with a narrow band of 1.40–1.44 eV and high absorption coefficients of over $1.00 \times 10^5 \text{ cm}^{-1}$, we investigated the blend miscibility and device performance of all-PSCs based on a wide-band-gap polymer donor, PM6. The PYT_M-based all-PSCs exhibit an excellent PCE of 13.44%, outperforming those with PYT_L (12.55%) and PYT_H (8.61%). Our results provide insight into polymer acceptor backbone and molecular mass and suggest guidelines to rationally select polymers for all-PSCs.

INTRODUCTION

Solution-processed polymer solar cells (PSCs), recognized as a promising technology of converting solar energy to electricity, have attracted much attention due to their advantages of flexibility, low-cost, light-weight, transparent, and easy of large-scale fabrication.^{1–6} Intense research efforts over the past years have provided a deeper understanding of the efficient photovoltaic materials,^{7–11} interface materials,^{12–14} and device engineering,^{5,15} now enabling fullerene-free PSCs with power conversion efficiencies (PCEs) beyond 16%. Among the various systems in non-fullerene PSCs,^{16,17} all-polymer solar cells (all-PSCs),¹⁸ which are composed of binary blends of conjugated polymer donor (P_D) and polymer acceptor (P_A), attract particular interest, because of enhanced polymer electronic structure tunability, excellent thermal stability, and mechanical bulk heterojunction (BHJ) film robustness.^{19–21} In addition, all-polymer system maintains a good compatibility with large-area manufacture during operation and stress testing protocols.^{22–24} Recently, the PCEs of all-PSCs have been dramatically enhanced to exceeding 11%.^{25,26} This progress is mainly resulting from optimal polymer design,^{27–30} BHJ morphology control,^{25,31–34} and device fabrication engineering.³⁵

Context & Scale

All-polymer solar cells (all-PSCs), composed of blends of polymer donor (P_D) and polymer acceptor (P_A), attract much attention. However, only a few all-PSCs have yielded the power conversion efficiency (PCE) values of >10%, mainly due to the lack of high-performance polymer acceptor and poor P_D-P_A pair miscibility because of the self-aggregation of polymers. Here, we reported a polymer acceptor PYT with a low optical band gap and a high absorption coefficient and established a friendly relationship between the average molecular weight (M_n) of PYT and P_D-P_A miscibility to get an ideal morphology. The medium M_n of PYT (PYT_M) leads to the suitable PM6:PYT_M pair miscibility. Consequently, the resultant device shows an impressive PCE of 13.44%, which is among the top values of all-PSCs. By this research, we point out the true potential of the polymer backbone and molecular mass to further improve the photovoltaic performance in all-PSCs.

In 1995, Friend and Heeger initially made pioneering independent studies on all-PSCs employed P_A CN-PPV (Poly[2,5-di(hexyloxy) cyanoterephthalylidene]).^{36,37} After that, many efforts have been devoted to the development of P_A materials, such as perylene diimide (PDI),^{29,38} naphthalene diimide (NDI),^{39–41} dicyanobenzo-thiadiazole moieties,^{42,43} B←N-bridged bipyridine,^{44–46} and their derivatives^{47,48} based copolymers to enhance the photovoltaic performance of all-PSCs. For instance, in 2007, Zhan et al. synthesized a high-mobility electron-transport polymer based on alternating PDI and dithienothiophene units,²⁷ which showed a PCE of over 1% when a polythiophene derivative as a donor was used. Furthermore, Sirringhaus and Loi independently pioneered all-PSCs based on the NDI-based P_A N2200 (poly[[N,N'-bis(2-octyldodecyl)-naphthalene-1,4,5,8-bis(dicarboximide)-2,6-diyl]-alt-5,5'-(2,2'-bithiophene)]).^{31,49} However, the NDI- and PDI-based polymer derivatives generally show low absorption coefficients in films, which limited their short-circuit current density (J_{sc}) in devices,^{38,39} even though the PCEs of 10%–11% of the N2200-based all-PSCs were achieved by carefully selecting polymer donors, processing solvents, and molecular weights.^{26,50,51} Another design approach to enhance the absorption coefficient and PCE was reported in 2017 by Li et al., who designed a fused-aromatic-ring-constructed P_A PZ1 (Poly[(2,2'-((2Z,2'Z)-((4,4,9,9-tetrahexadecyl-4,9-dihydro-s-indaceno[1,2-b:5,6-b']dithiophene-2,7-diyl)bis-(methanylylidene))bis(3-oxo-2,3-dihydro-1H-indene-2,1-diylidene)) dimalononitrile-alt-2,5-thiophene])).⁴³ However, PZ1 as well as its derivatives show the medium optical band gaps (E_g^{opt}) in the range of 1.55–1.62 eV.^{42,43,48} Obviously, further development of all-PSCs is hampered by the P_A materials.

Apart from the challenges reported above, achieving suitable BHJ microstructure is also a particularly challenging one for the all-polymer photovoltaic system because the reduced entropic contributions significantly suppress P_D - P_A pair miscibility.⁵² In general, poor P_D - P_A miscibility results in extreme donor-acceptor phase separation,^{27,53–56} limiting charge transport property and thereby promoting charge carrier recombination in the BHJ microstructure. The current studies show that achieving suitable P_D - P_A miscibility has an enormous impact on the whole process of converting solar light into electricity and consequently determines photovoltaic performance of all-PSCs.^{57–59} However, rational design of P_A has been elusive, because the photovoltaic performance is very sensitive to their number-average molecular weight (M_n) values, which has also been highlighted in all-PSCs.^{60–63} Overall, finding a P_A with a low-band-gap and high-absorption coefficient and establishing the friendly relationship between the M_n of polymer materials and P_D - P_A miscibility will be very important for the development of highly efficient all-PSCs.

Herein, we report a π -conjugated P_A PYT (Poly[(2,2'-((2Z,2'Z)-((12,13-bis(2-octyldodecyl)-3,9-diundecyl-12,13-dihydro[1,2,5]thiadiazolo[3,4e]thieno[2'',3'':4',5']thieno[2',3':4,5]pyrrolo[3,2-g]thieno[2',3':4,5]thieno[3,2-b]-indole-2,10-diyl)bis(methanylylidene))bis(3-oxo-2,3-dihydro-1H-indene-2,1-diylidene)) dimalononitrile-alt-2,5-thiophene)]) as shown in Figure 1A, composed of A-DAD-A constructed small molecule acceptor Y5-C20 as the key building block and thiophene as the linking unit. PYT possesses broad absorption with a narrow band gap of approximately 1.40–1.44 eV and high absorption coefficient of over $1.00 \times 10^5 \text{ cm}^{-1}$. In addition, we systematically investigate the effect of molecular weight of PYT on the blend morphology and photovoltaic performance of all-PSCs based on a wide-band-gap polymer PM6 (Poly[(2,6-(4,8-bis(5-(2-ethylhexyl-3-fluoro)thiophen-2-yl)-benzo[1,2-b:4,5-b']dithiophene))-alt-(5,5'-(1',3'-di-2-thienyl-5',7'-bis(2-ethylhexyl)benzo[1',2'-c:4',5'-c'] dithiophene-4,8-dione))]⁶⁴ as donor. The medium M_n of PYT (PYT_M) leads to the suitable PM6:PYT_M pair miscibility. Consequently, the PM6:PYT_M all-PSCs exhibit more

¹The Institute for Advanced Studies, Wuhan University, Wuhan 430072, China

²Beijing National Laboratory for Molecular Sciences, Beijing 100190, China

³Key Laboratory of Materials Processing and Mold (Zhengzhou University), Ministry of Education, Zhengzhou 450002, China

⁴These authors contributed equally

⁵Lead Contact

*Correspondence: min.jie@whu.edu.cn

<https://doi.org/10.1016/j.joule.2020.03.019>

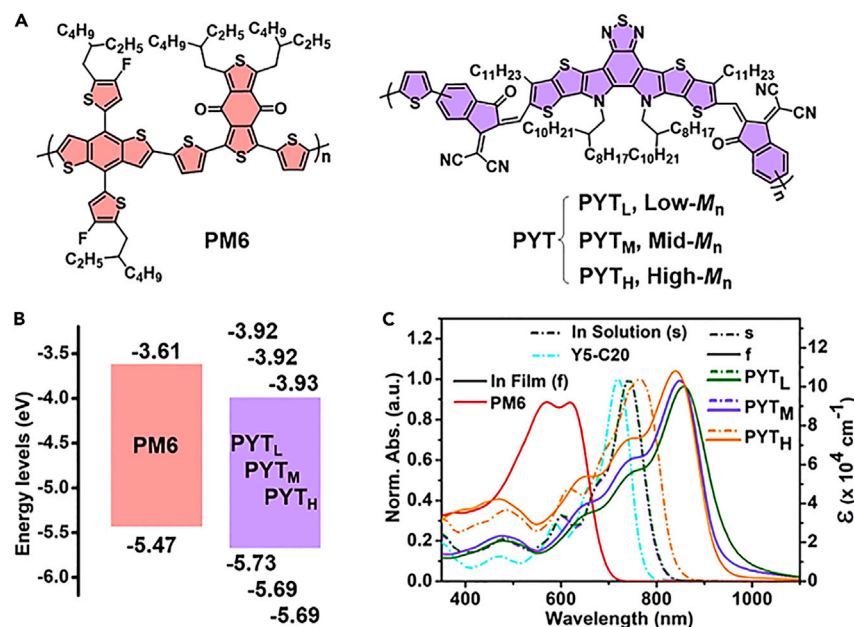


Figure 1. Molecular Structures: Electrochemical and Optical Properties

(A) Molecular structures of P_D PM6 and P_A PYT.

(B) Energy level diagram of PM6 and PYT series.

(C) Normalized absorption spectra of materials in dilute CF solution and the corresponding absorption coefficients in the thin films.

balanced charge transport property, less carrier recombination loss, and thus enhanced photovoltaic performance as compared to the other two photovoltaic systems based on the PYT with low and high molecular weight (PYT_L and PYT_H), respectively. Careful studies are also addressed how the relevant energy loss and blend microstructure determined the device performance. Importantly, the resultant PM6:PYT_M device shows an impressive PCE of 13.44%, which is among the top values of all-PSCs.

RESULTS AND DISCUSSION

Synthesis and Characterization of P_A PYT

The synthetic routes and chemical structures of the monomers and P_A PYT are depicted in Scheme S1 in the Supplemental Information. The synthetic details, nuclear magnetic resonance (NMR) spectra and mass spectrometry (MS) spectrum (Figures S1–S7; Supplemental Information) were given in Supplemental Experimental Procedures. The target polymer PYT (Figure 1A) was obtained through a still cross coupling reaction between Y5-C20-Br and 2,5-bis(trimethylstannyl)thiophene. PYT with different molecular weights were synthesized by controlling the reaction time in the Stille polycondensation. The relevant *M_n* and polydispersity index (PDI) of three PYT samples were determined to be 7.2 kg mol⁻¹ and 1.16 (low-*M_n*, PYT_L), 12.3 kg mol⁻¹ and 1.67 (mid-*M_n*, PYT_M), and 20.6 kg mol⁻¹ and 1.86 (high-*M_n*, PYT_H), respectively (Figure S8; Table S1). These data were determined by high-performance gel chromatography with polystyrene standards. These PYT series, including PYT_L, PYT_M, and PYT_H, show good solubility in common solvents (e.g., chloroform [CF], and *o*-dichlorobenzene [*o*-DCB]) and can be easily cast into uniform films.

The thermogravimetric analysis (TGA) measurements show that PYT series also have excellent thermal stability as evidenced by the high onset thermal

decomposition (5%) temperature of 300°C for PYT_L, 305°C for PYT_M, and 339°C for PYT_H, respectively (Figure S9). In addition, for PYT with different M_n , melting or glass transition was not observed in the differential scanning calorimetry (DSC) in the temperature range of room temperature (RT) to 300°C (Figure S10). The results indicate its good thermal stability characteristics and the amorphous nature of polymer PYT with different M_n . Besides, the energy levels of PM6 and PYT series were calculated, as shown in Figure 1B. The lowest unoccupied molecular orbital (LUMO) and highest occupied molecular orbital (HOMO) energy levels of PYT only have a minute difference (Figure S11; Table S2), suggesting the M_n has little impact on energy levels.

The ultraviolet-visible (UV-vis) absorption spectra of the three PYT series were measured in dilute CF solution and in solid film (Figure 1C), and the corresponding data are summarized in Table S3. In dilute solution, PYT_L exhibits a similar absorption spectrum to PYT_M, while the spectra of PYT_H are redshifted by approximately 23 nm to PYT_L and PYT_M, which can be attributed to the more obvious aggregation of polymer PYT caused by a high M_n of 20.6 kg mol⁻¹. It should be noted that the solution absorption spectra of PYT series show a redshift compared to the solution spectra of the small molecular acceptor Y5-C20 (Figure 1C), which results from the extended π -conjugated backbone of the polymers. Due to the π - π interactions formed in the solid films, the absorption spectra of the three PYT samples are all redshifted compared to their absorption spectra in solution. However, as shown in Figure 1C, the redshifts of PYT_L and PYT_M are 64 and 57 nm, respectively, while PYT_H are redshifted by only 27 nm, implying that PYT_L and PYT_M exhibit stronger π - π interactions than the PYT_H. In addition, as shown in Figure 1C, PM6 and PYT polymers showed complementary absorption and high absorption coefficient in the range of 350 to 900 nm that ensures good light harvesting ability to get a high J_{sc} .

Figure 1C further displays the UV-vis absorption spectra of the PYT series in films with the absorption coefficients of 1.00×10^5 cm⁻¹ for PYT_L, 1.03×10^5 cm⁻¹ for PYT_M, and 1.08×10^5 cm⁻¹ for PYT_H, respectively, indicating that the polymer acceptor PYT with larger M_n has higher absorption coefficient (ϵ).⁶⁵ Of note is that the PYT series show the broader optical absorption edge corresponding to band gaps (E_g^{opt}) of 1.40–1.44 eV compared to the Y5-C20 film with a E_g^{opt} of 1.49 eV (Figure S12A; Table S3), even though they exhibit the comparable absorption coefficients. Importantly, it is also found that the E_g^{opt} values (1.40–1.44 eV) of PYT series are much lower than those of the highly efficient polymer acceptors PZ1 (1.55 eV)⁴³ and P-BNBP-fBT (1.86 eV),⁴⁶ as shown in Figure S12B. Additionally, the absorption coefficients of PYT series are much higher than those of the efficient polymer acceptors N2200 with a ϵ of 3.48×10^4 cm⁻¹ at 697 nm²⁰ and DCNBT-IDT (Poly[5,6-dicyano-2,1,3-benzothiadiazole-alt-indacenodithiophene]) with a ϵ of 6.15×10^5 cm⁻¹ at 759 nm, respectively.⁶⁶ This analysis indicates that the PYT series-based devices should have great potential to absorb more energy photons, get higher J_{sc} , and offer increased power conversion efficiency, which will be discussed below.

We performed grazing incident wide-angle X-ray diffraction (GIWAXS) measurements to further investigate the molecular packing and crystallinity of the pristine PYT_L, PYT_M, and PYT_H films, as shown in Figure 2A. The corresponding in-plane (IP) and out-of-plane (OOP) line cuts of the corresponding neat films are exhibited in Figures 2B and 2C, respectively. The three polymer acceptors adopt a preferential face-on orientation showing more prominent (010) diffraction peaks located at $q_z = 1.64 \text{ \AA}^{-1}$ for PYT_L, $q_z = 1.64 \text{ \AA}^{-1}$ for PYT_M, and $q_z = 1.62 \text{ \AA}^{-1}$ for PYT_H in the

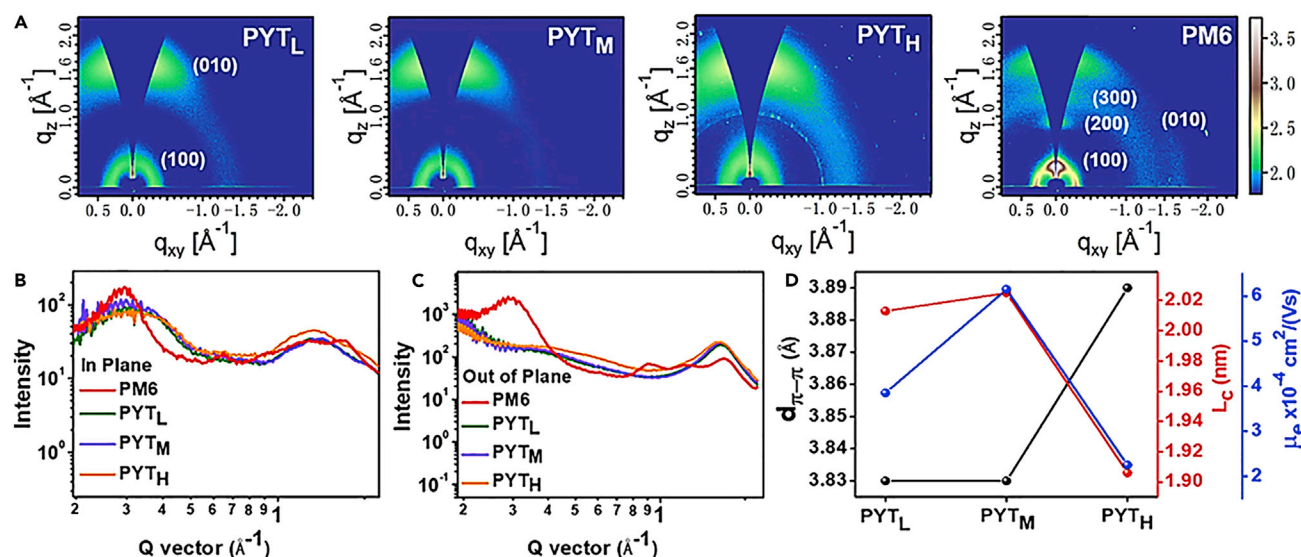


Figure 2. Morphological Analysis of the Pristine Films

(A) GIWAXS patterns for the pure films of PYT series and PM6.

(B and C) Scattering profiles of IP (B) and OOP (C) for PYT series.

(D) The $d_{\pi-\pi}$, L_c and μ_e of the PYT series as a function of M_n .

OOP direction (Table S4), which are similar to the reported Y5 acceptor that show preferential face-on ordering.⁶⁷ A closer look at them revealed that PYT_M shows a narrower angular distribution of OOP (010) peak, meanwhile PYT_H has more randomly oriented stacking, and PYT_L falls in between them, suggesting PYT_M had the strongest crystalline order compared to the others.⁶⁸ Besides, for the pristine donor polymer PM6, the (100), (200), and (300) diffraction peaks are present in the OOP direction, whereas the weak (010) peak appears in the IP direction, indicating that face-on and edge-on orientation exist simultaneously with respect to the substrate.

As the tightness of backbone stacking in the OOP direction is an important parameter for photovoltaic materials, we further calculate the OOP (010) π - π stacking distance ($d_{\pi-\pi}$) of all three acceptors (Table S4). The plot in Figure 2D exhibits $d_{\pi-\pi}$ as a function of M_n . It was found that a smaller $d_{\pi-\pi}$ of 3.83 Å was obtained in the PYT_L and PYT_M films than the neat PYT_H film. This indicates that PYT_L and PYT_M show stronger intermolecular aggregations, which is in accordance with the larger redshift in the absorption spectrum of their thin films as mentioned above. In contrast, the $d_{\pi-\pi}$ of PYT_H is significantly increased to 3.89 Å, indicating the unfavorable molecular π - π stacking. Apart from the $d_{\pi-\pi}$, we also use the full-width at half-maximum of the OOP (010) peak to analyze the π - π coherence length (L_c). As shown in Figure 2D, the L_c values of the three acceptors are 2.01 nm for PYT_L, 2.03 nm for PYT_M, and 1.91 nm for PYT_H, respectively, and PYT_M clearly shows the most ordered features.

Generally, the π - π stacking distance and coherence length results imply the charge transport characteristics of the polymer materials. Thus, the electron mobilities of neat films of these three polymer acceptors as a function of M_n were measured using the space-charge-limited-current (SCLC) method (Figure S13 for electron-only device). The electron mobility of PYT_M is $6.15 \times 10^{-4} \text{ cm}^2 \text{ V}^{-1} \text{ s}^{-1}$, which is higher than those for PYT_L ($3.85 \times 10^{-4} \text{ cm}^2 \text{ V}^{-1} \text{ s}^{-1}$) and PYT_H ($2.25 \times 10^{-4} \text{ cm}^2 \text{ V}^{-1} \text{ s}^{-1}$). As shown in Figure 2D, the electron mobility in these acceptors

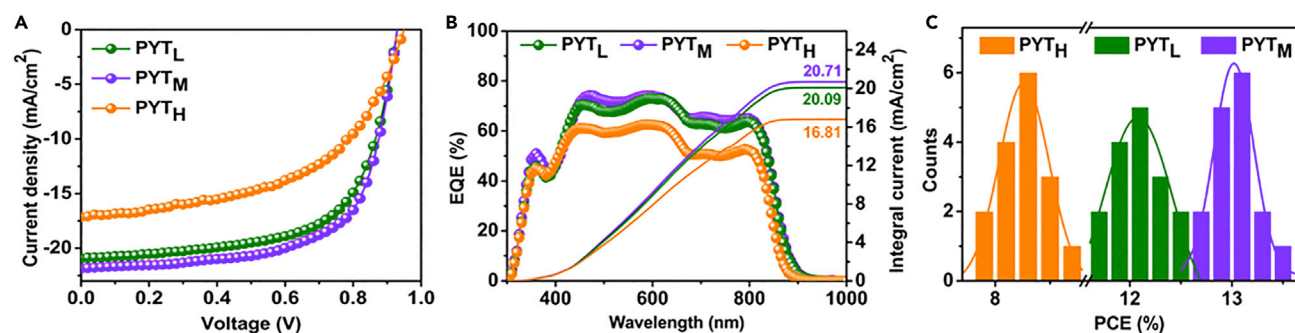


Figure 3. Photovoltaic Characteristics of the PYT-Based All-PSCs

(A) J-V curves of the PYT-based all-PSCs.

(B) EQE curves of the PYT-based all-PSCs.

(C) Histograms of the PCE counts for 16 individual PYT-based devices.

was found to be positively correlated with L_c and also related to $d_{\pi-\pi}$, i.e., the PYT_M with larger L_c and smaller $d_{\pi-\pi}$ has higher electron-only mobility. The results are not only associated with the above-discussed absorption spectra measurements but also imply that PYT_M is inferred to have much stronger molecular packing properties and electrostatic interactions as compared to the PYT_L and PYT_H. It should be noted that although the PYT_L and PYT_M samples show the similar $d_{\pi-\pi}$ spacing and L_c values, the slightly higher electron mobility of PYT_M compared to that of PYT_L is probably attributed to the slightly stronger preferential face-on molecular packing orientation and the different interface morphologies between the pristine films and buffer layers. Thus, it can be predicted that the PYT series as a function of M_n will lead to great changes in optoelectronic property, active layer morphology, charge transport property, and photovoltaic performance.

Photovoltaic Performance of All-PSCs

To explore the influence of the PYT series with different M_n on the photovoltaic performance, all-PSCs with a conventional-type structure of indium tin oxide (ITO)/poly(3,4-ethylenedioxythiophene)poly(styrenesulfonate)PEDOT:PSS/PM6:PYT series/PDI functionalized with amino N-oxide (PDINO)/Al were fabricated. To ensure the M_n of PYT as the unique variable on subsequent tests, the device fabrication parameters, such as D/A weight ratio, material concentration, solvent, and solvent additive, were controlled to the same. Optimized performance was achieved with the same D/A weight ratio of 1:1.2 for all the PYT series and the 0.5 vol % 1-chloronaphthalene (CN) as additive. The detailed procedures for the device fabrication were described in [Supplemental Experimental Procedures](#). The detailed photovoltaic performance of the investigated PM6:PYT all-PSCs based on different spin speeds are shown in [Figures S14–S16](#), and the related photovoltaic parameters are summarized in [Tables S5–S7](#). Additionally, [Figure 3A](#) plots the current density-voltage (J-V) curves of the corresponding best-performing solar cells based on the PYT series as acceptors, and [Table 1](#) listed the detailed photovoltaic characteristics of all-PSCs fabricated with the same conditions. All-PSCs based on PM6:PYT_M exhibit the highest PCE of 13.44% with an open circuit voltage (V_{oc}) of 0.93 V, a J_{sc} of 21.78 mA/cm², and a fill factor (FF) of 66.33%. Notably, the J_{sc} and PCE values of the PM6:PYT_M photovoltaic systems are the highest values reported in literature for all-PSCs based on different polymer acceptors as provided in [Figure S17](#). Of note is that the promising photovoltaic performance of the PM6:PYT_M system probably results from the low energy loss, which will be discussed below. Slightly lower performance is found for the PM6:PYT_L

Table 1. Summary of Photovoltaic Parameters of the Optimized All-PSCs

Devices	V_{OC} (V)	J_{SC} (mA/cm ²)	$J_{SC,EQE}^a$ (mA/cm ²)	FF (%)	PCE (PCE ^b) (%)
PM6:PYT _L	0.93	20.92	20.09	64.51	12.55 (12.02 ± 0.53)
PM6:PYT _M	0.93	21.78	20.71	66.33	13.44 (13.03 ± 0.41)
PM6:PYT _H	0.95	17.14	16.81	52.91	8.61 (8.29 ± 0.32)

^a $J_{SC,EQE}$ represents the integrated current density obtained from EQE spectra.

^bThe average PCE values with standard deviations were obtained from 16 devices.

devices with a PCE of 12.55%. However, a much lower PCE of 8.61% was obtained for the PM6:PYT_H devices, mainly due to lower J_{SC} and FF values. Furthermore, as compared to PYT_L- and PYT_M-based devices with the J_{SC} values for 20.92 and 21.78 mA cm⁻², respectively, its lower J_{SC} value (17.14 mA cm⁻² for the device based on PYT_H) is confirmed by external quantum efficiency (EQE) measurements for the best devices (Table 1). As compared to the EQE spectra of the PM6:PYT_H device, the PYT_L- and PYT_M-based devices not only possess the increased EQE in the entire absorption range but also show the redshifted EQE spectra.

Figure S18 exhibits the trend in device photocurrent density (J_{ph}) measured at -5V with the reverse photocurrent ($J_{ph} = J_L - J_D$) being defined as the difference between the dark (J_D) and the light current density (J_L) under one sun.⁶⁹ The relative change between J_{sc} and J_{ph} (-5V) is found to be the smaller for the PYT_L- and PYT_M-based devices exhibiting negligible voltage dependent recombination in contrast to the PM6:PYT_H device. Additionally, PYT_L- and PYT_M-based systems show a photocurrent of approximately 23 mA cm⁻² at -5 V, indicating comparable photogeneration rates. In contrast, the PYT_H-based blend exhibits a lower photogeneration rate with a J_{ph} of 19.04 mA cm⁻² at -5 V. Since the three blends based on PYT with different M_n possess very similar absorption spectrum and absorption coefficients as shown in Figure S19, the absorption properties were not the primary cause of the different J_{sc} values (Table 1). Thus, the relative low J_{sc} and FF values in PM6:PYT_H devices indicating that this photovoltaic system possess the poor physical mechanisms and unsuitable blend morphology with efficient carrier extraction, which will be discussed below.

Exciton and Carrier Dynamics

The selection of molecular weight enables changing the D/A interfacial area and fine-tuning the molecular ordering. This, in turn, is likely to sensitively change the fundamental photo-physical processes. Thus, we first investigated PL spectra under 639 nm photo-excitation to understand the influence of the M_n values of PYT on the exciton dissociation and the efficiency of exciton separation in the corresponding blends. As provided in Figure S20, PL spectroscopy presented quenching efficiencies of 77.6% for PM6:PYT_L blend and 80.4% for PM6:PYT_M blend, respectively. However, the quenching efficiency of PM6:PYT_H blend was only 52.2%, indicating much exciton was useless for charge generation, which can be the limiting factor for the low photocurrent of the devices (Figure 3A). Notably, these relatively modest PL quenching efficiencies of the PM6:PYT_L and PM6:PYT_M blends can be attributed most probably to the large domain size and high crystallinity of PYT_L and PYT_M, resulting in significant polymer exciton decay to ground during exciton diffusion to the P_D-P_A interface. This exciton decay to ground corresponds to an approximately 20% quantum efficiency loss, and is likely to be the main reason of the subunit maximal EQE data (Figure 3B). In addition, the unsuitable PM6:PYT_H blend with larger phase separation discussed below indicates the obvious quantum efficiency loss.⁶⁹ Further topographical characterization can shed light on this issue, which

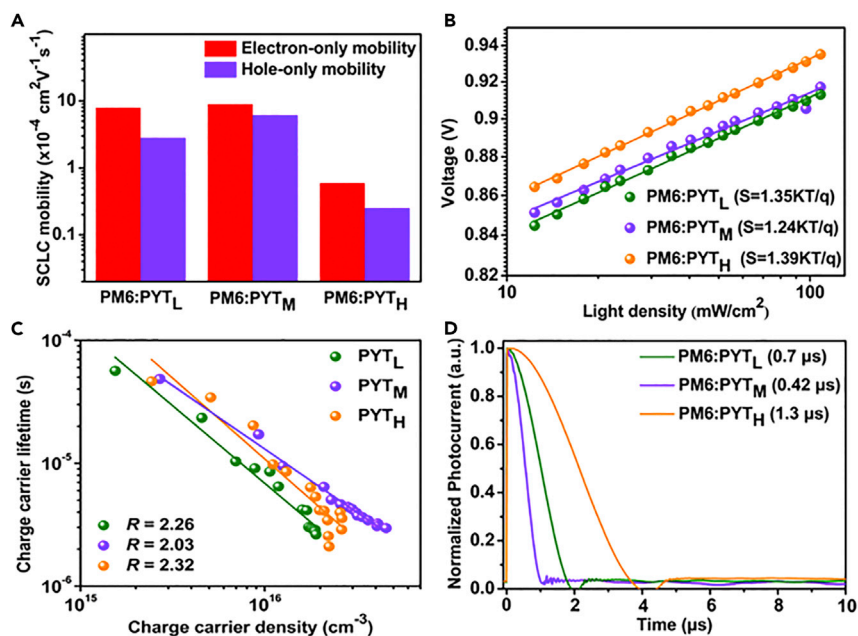


Figure 4. Charge Generation, Transport, Extraction, and Recombination

(A) The hole and electron mobilities of the PYT-based blend films.

(B) Measurement of V_{oc} versus light intensity for the devices.

(C) Charge carrier lifetime τ , obtained from TPV, as a function of charge density n , calculated from CE under V_{oc} conditions (from 0.15 to 2.50 suns). The solid lines represent linear fits of the data.

(D) Normalized TPC data for the relevant devices. The illumination pulse intensity was 150 mW cm^{-2} (light pulse of 50 μs).

we will systematically discuss in the last section. Here, we further calculated the exciton dissociation probabilities ($P(E, T), P(E, T) = \frac{J_{ph}}{J_{sat}}$, where J_{sat} is the saturation current density), which can be used to assess the exciton dissociation and charge collection efficiency in the corresponding devices. The $P(E, T)$ for the three types of devices were 95.0% (PM6:PYT_L blend), 95.9% (PM6:PYT_M blend), and 90.2% (PM6:PYT_H blend), respectively. Here, the exciton dissociation probabilities (charge collection efficiencies) in the relevant devices, in varying degrees, are higher than those of PL quenching efficiencies of the corresponding BHJ blends. On the one hand, this variation in percentage trend may originate from the intrinsic difference between the PL method for measuring exciton dissociation efficiency from a BHJ blend and the $P(E, T)$ model with an actual photovoltaic device. On the other hand, the morphology variation in the film and device may also be a factor, and the various physical mechanisms cannot be totally ruled out. Overall, the PM6:PYT_M device shows the highest J_{ph}/J_{sat} value, indicating the more efficient processes of exciton dissociation and charge collection than the other two types of devices.

Then, to gain deeper insight into the impact of M_n on charge transport in the corresponding blends, SCLC method was also used to map out the charge carrier mobilities investigated by analyzing the J - V characteristics of single carrier devices (Figure S21 for hole-only device and Figure S22 for electron-only device). The hole mobility of PM6:PYT_M blend is $6.12 \times 10^{-4} \text{ cm}^2 \text{ V}^{-1} \text{ s}^{-1}$, which is approximately twice higher than that of PM6:PYT_L blend ($2.81 \times 10^{-4} \text{ cm}^2 \text{ V}^{-1} \text{ s}^{-1}$) and over one order higher than that of PM6:PYT_H blend ($2.49 \times 10^{-5} \text{ cm}^2 \text{ V}^{-1} \text{ s}^{-1}$). Of note is that the neat PM6 film shows a hole mobility of $6.91 \times 10^{-4} \text{ cm}^2 \text{ V}^{-1} \text{ s}^{-1}$, implying that the

PYT_H added in the corresponding blend seriously disrupted the hole transport channel. In addition, the average electron mobilities of PM6:PYT_L and PM6:PYT_M blends are 7.88×10^{-4} and $8.91 \times 10^{-4} \text{ cm}^2 \text{ V}^{-1} \text{ s}^{-1}$, respectively, which is more than one order higher than that of PM6:PYT_H blend ($5.92 \times 10^{-4} \text{ cm}^2 \text{ V}^{-1} \text{ s}^{-1}$). In particular, the PM6:PYT_M blend showed balanced hole and electron mobilities with a μ_h/μ_e value of 0.69, which was closer to 1 than to 0.36 and 0.42 for PM6:PYT_L and PM6:PYT_H blends, respectively. Besides, as shown in Figure 4A, the relatively low mobilities of PM6:PYT_H blend lead to reduced FF values in devices. The sharply reduce of μ_h and μ_e in PM6:PYT_H blends should be due to the excessive aggregation of PYT_H that isolated the acceptor and donor domains, leading to the poor charge carrier transport.

Trap-assisted recombination losses in these blends were first detected by V_{oc} versus light intensity curves in Figure 4B. The light intensity dependence of V_{oc} data are fitted to the linear law: $V_{oc} \propto \frac{nkT}{q \ln I_{light}}$,⁷⁰ where k , T , and q are the Boltzmann constant, the temperature in Kelvin and the elementary charge, respectively. The semi-logarithmic plot of V_{oc} depends linearly on the light intensity with a slope S of kT/q . In general, when S is larger than kT/q , monomolecular recombination and trap-assisted recombination are involved. The slopes were calculated to be 1.35, 1.24, and 1.39 kT/q for PM6:PYT_L, PM6:PYT_M, and PM6:PYT_H, respectively, indicating fewer monomolecular and trap-assisted recombination in the PM6:PYT_M device than the PYT_L- and PYT_H-based devices. In addition, we evaluated the non-geminate recombination order R with the transient photovoltage (TPV) and charge extraction (CE) techniques. The R value ($R = \lambda + 1$) can be calculated via the equation $\tau = \tau_0 \left(\frac{n_0}{n} \right)^\lambda$,⁷⁰ where τ_0 and n_0 are constants and λ is the so-called recombination exponent. As shown in Figure 4C, we plot the charge carrier lifetimes obtained from TPV measurements (Figure S23) as a function of charge carrier density obtained from CE measurements (Figure S24). A lower recombination order value ($R = 2.03$) for the PM6:PYT_M device was achieved, which can be directly correlated to the effective exciton dissociation probability and the spatial uniform charge carrier distributions through active layer. It also strongly implies the lower carrier recombination loss than the other two types of devices with the R values of 2.26 for PM6:PYT_L and 2.32 for PM6:PYT_H. Besides, apart from the J_{ph} and J_{sat} measurements discussed above, more detailed information about the CE property in the devices can be performed by using transient photocurrent (TPC) measurements. As provided in Figure 4D, the CE time are 0.70 μs for the PM6:PYT_L blend, 0.41 μs for the PM6:PYT_M blend, and 1.3 μs for the PM6:PYT_H blend, respectively. The shorter extraction lifetime suggests that photo-generated carriers are extracted more efficiently in the PM6:PYT_M device than the PYT_L- and PYT_H-based devices. As a result, the reduced charge recombination and extraction lifetime afforded the increased FF and J_{sc} values in the PM6:PYT_M device as compared with the other two types of devices.

Energetic Losses

In order to investigate the intrinsic reasons that cause the dramatically changed photovoltaic performance of the devices, here, we systematically studied the energy loss (E_{loss}) issue of the all-PSCs based on the polymer acceptors PYT with different M_n . We first tested the electroluminescence (EL) of PM6:PYT devices with active layer thicknesses of $100 \pm 5 \text{ nm}$ that was measured under a constant current injection density of 20 mA cm^{-2} . As shown in Figure S25, the higher EL intensity of PM6:PYT_M device as compared to the PM6:PYT_L and PM6:PYT_H devices indicates a relatively higher emissive quantum yield for the charge-transfer (CT) state^{71,72}

Table 2. Detailed E_{loss} and V_{loss} Parameters of the All-PSCs Based on PM6:PYT Blends

Devices	E_{gap} (eV)	V_{oc} (V)	E_{loss} (eV)	$V_{\text{oc}}^{\text{SQ}^a}$ (V)	ΔE_1 (eV)	$V_{\text{oc}}^{\text{rad}^b}$ (V)	ΔE_2^c (eV)	ΔE_3^d (eV)
PM6:PYT _L	1.457	0.93	0.532	1.199	0.258	1.154	0.045	0.229
PM6:PYT _M	1.466	0.93	0.528	1.207	0.259	1.148	0.058	0.210
PM6:PYT _H	1.492	0.95	0.544	1.232	0.260	1.170	0.062	0.222

^a $V_{\text{oc}}^{\text{SQ}}$: Schokley-Queisser limit to V_{oc} .

^b $V_{\text{oc}}^{\text{rad}}$: radiative limit to V_{oc} , measured using EQE_{EL}.

^c ΔE_2 ($\Delta V_{\text{oc}}^{\text{rad}}$): voltage losses due to non-ideal absorption (it was calculated from EL and FTPS measurements).

^d ΔE_3 ($\Delta V_{\text{oc}}^{\text{non-rad}}$): voltage losses due to non-radiative recombination only.

for PM6:PYT_M devices. Furthermore, we quantified the optical band gaps (E_{gap}) of all the blend films based on the cross point between the absorption spectra and EL of blends.⁷³ As shown in Figure S26, the E_{gap} of PM6:PYT_L, PM6:PYT_M, and PM6:PYT_H blends is 1.457, 1.466, and 1.492 eV, respectively. The total E_{loss} was further determined according to $E_{\text{loss}} = E_{\text{gap}} - qV_{\text{oc}}$, where E_{gap} is determined from the EQE onset,^{74–76} and the results are summarized in Table 2. We note that the M_n of PYT acceptors have obvious impacts on E_{loss} , leading to values of 0.532 eV for PYT_L, 0.528 eV for PYT_M, 0.544 eV for PYT_H, respectively. As far as we know, the photon energy loss may facilitate charge separation and improve the exciton dissociation efficiency.^{72,75} Here, we provide how the EQE relates to E_{loss} for a range of successful all-polymer photovoltaic systems, as exhibited in Figure S27. Here, we also present the result of the optimized PM6:PYT_M device with a E_{loss} of 0.472 eV (Table S9). Although the E_{loss} of the PM6:PYT_M devices is the smallest among the published all-polymer systems, this system shows a high EQE of 74%, which is better than most all-polymer systems provided in Figure S27. In addition, there are several mechanisms that can contribute to a low E_{loss} while maintaining a high EQE. Among these are reducing energetic disorder, eliminating defects that can trap charges, reducing the D/A interface area and so on.^{71,72,74,75,77} As expected, further material design and morphology control is imperative to increase the EQE and efficiency of all-PSCs meanwhile keep a low photo energy loss.

In order to probe the impact of M_n of PYT acceptors on the E_{loss} of devices, we carried out the Fourier transform photocurrent spectroscopy (FTPS) and EL measurements⁷⁷ of the three devices (Figure 5). The detailed components of E_{loss} can be categorized into three parts based on the SQ limit, as shown in Equation 1.⁷⁸

$$E_{\text{loss}} = E_{\text{gap}} - qV_{\text{oc}} = \Delta E_1 + \Delta E_2 + \Delta E_3$$

$$= (E_{\text{gap}} - qV_{\text{oc}}^{\text{SQ}}) + (qV_{\text{oc}}^{\text{SQ}} - qV_{\text{oc}}^{\text{rad}}) + (qV_{\text{oc}}^{\text{rad}} - qV_{\text{oc}}) \quad (\text{Equation 1})$$

Through disentangling the different loss parts to the total E_{loss} (here, $E_{\text{loss}} = \Delta E_1 + \Delta E_2 + \Delta E_3$ with ΔE_1 arising from the loss related to the SQ-limit, and ΔE_2 and ΔE_3 related to the loss via radiative recombination below band gap and non-radiative recombination, respectively),⁷⁹ we found ΔE_2 and ΔE_3 in the three devices are obviously affected, as shown in Table 2. Among them, the values of ΔE_2 gradually increase as the molecular weight of PYT increases. The large ΔE_2 value of 0.062 eV in the PM6:PYT_H device mean the radiative recombination loss from the absorption below the band gap is significant. The ΔE_3 values were 0.229 eV for PM6:PYT_L device, 0.210 eV for PM6:PYT_M device, and 0.222 eV for PM6:PYT_H device, respectively. It is found that the PM6:PYT_M device showed the reduced ΔE_3 in comparison with the other two types of devices. Of note, both radiative and non-radiative losses of these devices are relatively low (ΔE_2 of 0.04–0.07 and ΔE_3 of 0.21–0.23 eV), probably resulting from the low driving energy ($\Delta E_{\text{S}_1, \text{CT}}$), which is generally assumed to be correlated to the difference in the HOMO energies of the D/A materials ($\Delta E_{\text{HOMO}} =$

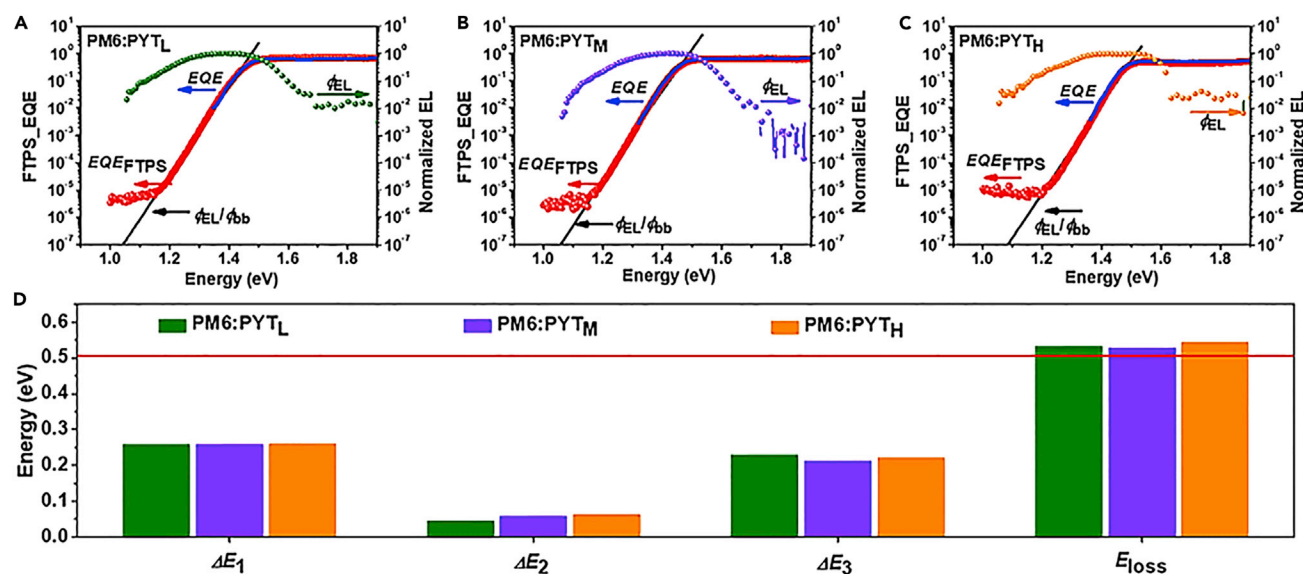


Figure 5. Energy Loss Analysis in All-PSCs

(A–C) Semi-logarithmic plots of normalized EL, measured EQE and EQE calculated by FTPS (EQE_{FTPS}) as a function of energy for devices based on PM6:PYT_L (A), PM6:PYT_M (B), and PM6:PYT_H (C). The ratio of $\phi_{\text{EL}}/\phi_{\text{bb}}$ was used to plot the EQE in the low-energy regime (black line), where ϕ_{EL} and ϕ_{bb} represent the emitted photon flux and the room-temperature blackbody photon flux, respectively. Of note is that $\phi_{\text{EL}}/\phi_{\text{bb}}$ follows experimental EQE_{FTPS} faithfully at higher energies as expected from reciprocity.

(D) E_{loss} and its detailed three parts of ΔE_1 , ΔE_2 , and ΔE_3 values.

$E_{\text{HOMO,D}} - E_{\text{HOMO,A}}$).⁷⁹ On the basis of the smaller non-radiative recombination loss in the PM6:PYT_M device, it suggests that with the incorporated P_A PYT with a medium M_n having a good compatibility with the polymer donor (P_D) PM6, not only the PL quenching efficiency and charge transport property are improved, but also the energetic disorder at the D/A interface is decreased, which promotes interfacial charge transfers and dissociation. These merits as mentioned above likely lead to the enhancement of J_{sc} and FF in the PM6:PYT_M devices as compared to the other two types of devices, especially for the PM6:PYT_H devices.

Overall, the results of the exciton dissociation properties and probabilities coupled with the analysis of the charge carrier mobilities and the carrier recombination dynamic as well as the evaluation of energy losses in these devices provide detailed insight into subtle mechanisms being responsible for device parameters as a function of M_n . Actually, these relationships between physical dynamic and device performance are mainly determined by the morphology characterizations, which will be discussed in detail later.

Structural and Morphological Properties of Active Layers

From our spectroscopic measurements thus far, we have found that the PM6:PYT_H blend suffered from exciton harvesting limitations, whereas exciton harvesting and charge generation can be considered efficient in the PM6:PYT_L and PM6:PYT_M blends. We have also demonstrated that the PM6:PYT_H device endured poorer charge transport and extraction, and more carrier trapping than the PM6:PYT_L and PM6:PYT_M devices. To further demonstrate the effect of different M_n on the above-mentioned photovoltaic performance and physical dynamics in the three devices and correlate them to the corresponding morphological characterizations, tapping-mode atomic force microscopy (AFM) and GIWAXS have been carried out.

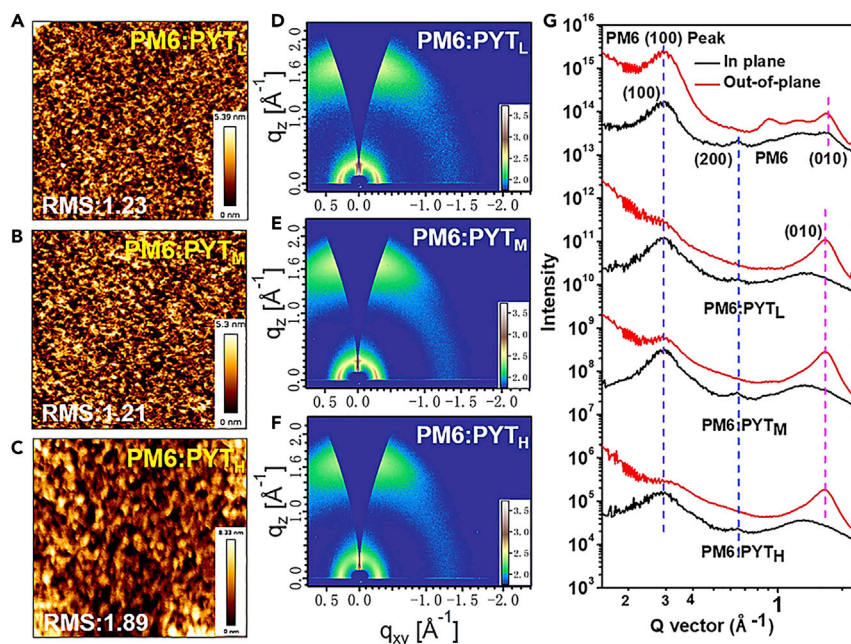


Figure 6. Morphological Properties of Active Layers

(A–C) Contact mode AFM surface scans ($5 \times 5 \mu\text{m}^2$) of PM6:PYT_L (A), PM6:PYT_M (B), and PM6:PYT_H (C). (D–F) GIWAXS patterns for PM6:PYT_L (D), PM6:PYT_M (E), and PM6:PYT_H (F). (G) Scattering profiles of IP and OOP for PM6 and PM6:PYT blends.

Both PM6:PYT_L and PM6:PYT_M blends exhibit a smooth surface with a small root mean square (RMS) roughness of 1.23 and 1.21 nm, respectively (Figures 6A and 6B). In addition, it can be found that these two blends form defined phase separation with a bi-continuous interpenetrating network, which is beneficial to suppress the exciton recombination and improve the charge separation and transport properties as mentioned above. However, further increasing M_n of PYT results in more rough film (a RMS roughness of 1.89 nm) with significant phase separation and large domain size (Figure 6C). Note that the large domain sizes on the length scale of hundred nanometers in the PM6:PYT_H blend can seriously result in regions of charge trapping, poor charge separation process, and other losses discussed earlier, which significantly influences the J_{sc} and FF values of the PM6:PYT_H devices. In order to further analyze the different origins of the blend morphologies and compare the compatibility of the P_D and PYT with different M_n , we delineate the critical role of miscibility expressed in terms of the Flory-Huggins interaction parameter (χ).⁸⁰ The χ values, between donor and acceptors, are calculated from experimentally measured contact angles (Figure S28, using two solvents, water and ethylene glycol [EG]), and summarized in Table S10. As a consequence, the calculated χ values for PYT_L, PYT_M, and PYT_H showed 0.003, 0.066, and 0.200 for blended with PM6. It means that the PM6:PYT_L and PM6:PYT_M blends have a more miscible due to relatively low χ values compared to that of PM6:PYT_H blend. In contrast, a high χ value of 0.200 implies the severe phase segregation in the PM6:PYT_H system, which have been demonstrated by the above-discussed AFM image (Figure 6C). These trends were also supported by comparing the PL quenching efficiency of the three different blends (Figure S20). Thus, it is expected that a proper phase separation of the polymer blends is very important to realize high-performance all-PSCs.

To further investigate the crystallization at nanoscale, GIWAXS measurements of the PM6:PYT_L (Figure 6D), PM6:PYT_M (Figure 6E), and PM6:PYT_H (Figure 6F) blends

were carried out. As mentioned above, PM6 adopts bimodal distribution, evidenced by the simultaneous appearance of (100) lamellar diffraction and (010) π - π stacking peak along both IP and OOP directions, while the three polymers showed a preferential face-on molecular packing orientation (Figures 2B and 2C). Interestingly, for the blends, the (010) and (100) peaks are located at both, the OOP and IP directions (Figure 6G), respectively. When compared with the pristine films, the blends of PYT_L and PYT_M showed a stronger intensity of (010) peaks, while the PYT_H exhibited weaker face-on stacking. The GIWAXS data of (100)-IP peaks and (010)-OOP peaks using the Gaussian function are fitted first, as shown in Figures S29 and S30, respectively. And the relevant fitting data are summarized in Tables S11 and S12, respectively. The detailed results of the (100)-IP peak's fitting patterns are in good agreement with the GIWAXS measurements of neat films. This indicates that PM6 and PYT within the blend have kept the same orientation as the pure film, giving their preferential orientations simultaneously. In addition, with Gaussian fitting, there is only one peak found for (010)-OOP peaks in relevant blends. The (010)-OOP peaks of PYT series have a better fit, but not exactly fit, as shown in Figure S30. In Table S12, the data are also well match with the GIWAXS data of neat film.

In Figure 6G, we can also find the lamellar packing peaks were still clear in the PM6:PYT_L and PM6:PYT_M blends, demonstrating (010)-OOP peaks of PYT_L and PYT_M, and (100) peak from PM6, respectively, at the same position as in the pristine materials, thereby implying that when blended with PM6, PYT_L and, PYT_M molecules favored to form more ordered arrangement. In contrast, the PM6:PYT_H exhibits a different behavior, indicating a relatively strong interaction between PM6 and PYT_H because of its relatively longer rigid backbones.

It should be noted that the PM6:PYT_M have the smallest (100) lamellar stacking distance of 21.37 Å and (010) π - π stacking distance of 3.78 Å (Table S13) as compared to the PM6:PYT_L and PM6:PYT_H blends, indicating that it adopted closer and more ordered molecular orientation. In addition, the PM6:PYT_M blend remains in the preferred (200) lamellar diffraction of PM6 along the IP direction, responsible for the good charge transport of the all-PSCs. Besides, the coherence length (L_c) values, determined from the full-width-at-half-maximum of X-ray reflection (the Scherrer equation), are 19.5 Å for the PM6:PYT_L blend, 19.5 Å for the PM6:PYT_M blend, and 17.5 Å for the PM6:PYT_H blend, respectively (Table S13). Since the L_c is related to the crystalline size and lattice order,⁸¹ the larger L_c values of the corresponding PM6:PYT_L and PM6:PYT_M blends have less grain boundaries and therefore render better charge transport properties than the PM6:PYT_H blend. Since the PM6:PYT_H blend has the smallest coherence length of 17.5 Å, which are identical to the trend of SCLC analysis (Figure 4A). It is noteworthy that the smaller L_c value of the PM6:PYT_H blend can be the critical fact of the poorer J_{sc} and FF values as compared to those of the PYT_L- and PYT_M-based blends (Figure 3A; Table 1). Thus, it can be seen that the morphological characterizations of these blends are consistent with the physical dynamics and device performance of all-PSCs observed above.

Conclusion

In this work, applying a fused-ring electron acceptor Y5-C20 as the key building block and thiophene as the π -bridges, we designed and synthesized a π -conjugated P_A PYT. In particular, the absorption coefficients of PYT gradually increase as its molecular weight increases, but the absorption edge of PYT blueshifts. These drive us to synthesize a series of PYT polymer acceptors with controlled

M_n values for fine-tuning the molecular crystallinity and P_D - P_A miscibility. When fabricated into all-PSCs with PM6, we observed a clear molecular weight dependence on device performance. Optimized devices based on PYT_L , PYT_M , and PYT_H exhibits PCEs of 12.55%, 13.44%, and 8.61%, respectively. As compared to PM6: PYT_L and PM6: PYT_H systems, the higher device efficiency of PYT_M originates from the more efficient exciton dissociation and charge generation, higher carrier mobility, faster CE in combination with suppressed carrier recombination, and reduced energy loss and is further assigned to a better blend morphology with suitable phase separation. Whereas PM6: PYT_H system shows a very poor device efficiency, mainly resulting from the poor morphology with large domains observed above. The presented results not only point out a promising design strategy of polymer acceptor tuned through molecular engineering on the fused-ring electron acceptor units of the small molecule acceptors but also highlight the importance of the molecular weight of polymers as a vital factor for high-performance all-PSCs. Therefore, the molecular backbone of polymer as well as its molecular mass are necessary to carefully understand their true performance potential and promote further advances in the field of PSCs.

EXPERIMENTAL PROCEDURES

Full details of experimental procedures can be found in the [Supplemental Information](#).

SUPPLEMENTAL INFORMATION

Supplemental Information can be found online at <https://doi.org/10.1016/j.joule.2020.03.019>.

ACKNOWLEDGMENTS

This work was financially supported by the National Natural Science Foundation of China (NSFC) (grant no. 21702154 and 51773157). We also thank the support of the opening projects of Key Laboratory of Materials Processing and Mold and Beijing National Laboratory for Molecular Sciences (BNLMS201905).

AUTHOR CONTRIBUTIONS

W.W. and Q.W. conceived the ideas and coordinated the work. Q.W. fabricated all the solar cell samples and conducted the measurements. W.W. and Y.W. contributed to the acceptor polymer-based all-polymer solar cell design and data analysis. R.S. performed the transient measurement unit (TMU) and AFM measurements, and J.G. performed FTPS and PL measurements. M.S., W.Y., and H.L. performed devices morphology measurements. W.W., Q.W., and J.M. contributed to manuscript preparation, and W.W. and Q.W., supervised by J.M., conceived and directed the project. All authors commented on the manuscript.

DECLARATION OF INTERESTS

The authors declare no competing interests.

Received: December 4, 2019

Revised: February 16, 2020

Accepted: March 23, 2020

Published: April 16, 2020

REFERENCES

- Yu, G., Gao, J., Hummelen, J.C., Wudl, F., and Heeger, A.J. (1995). Polymer photovoltaic cells: enhanced efficiencies via a network of internal donor-acceptor heterojunctions. *Science* 270, 1789–1791.
- Cui, Y., Wang, Y., Bergqvist, J., Yao, H., Xu, Y., Gao, B., Yang, C., Zhang, S., Inganäs, O., Gao, F., and Hou, J. (2019). Wide-gap non-fullerene acceptor enabling high-performance organic photovoltaic cells for indoor applications. *Nat. Energy* 4, 768–775.
- Kim, Y., Cook, S., Tuladhar, S.M., Choulis, S.A., Nelson, J., Durrant, J.R., Bradley, D.D.C., Giles, M., McCulloch, I., Ha, C.-S., and Ree, M. (2006). A strong regioregularity effect in self-organizing conjugated polymer films and high-efficiency polythiophene: fullerene solar cells. *Nat. Mater.* 5, 197–203.
- Fan, B., Zhong, W., Ying, L., Zhang, D., Li, M., Lin, Y., Xia, R., Liu, F., Yip, H.L., Li, N., et al. (2019). Surpassing the 10% efficiency milestone for 1-cm² all-polymer solar cells. *Nat. Commun.* 10, 4100.
- Wu, Q., Guo, J., Sun, R., Guo, J., Jia, S., Li, Y., Wang, J., and Min, J. (2019). Slot-die printed non-fullerene organic solar cells with the highest efficiency of 12.9% for low-cost PV-driven water splitting. *Nano Energy* 61, 559–566.
- Guo, J., and Min, J. (2019). A cost analysis of fully solution-processed ITO-free organic solar modules. *Adv. Energy Mater.* 9, 1802521.
- Sun, C., Pan, F., Bin, H., Zhang, J., Xue, L., Qiu, B., Wei, Z., Zhang, Z.G., and Li, Y. (2018). A low cost and high performance polymer donor material for polymer solar cells. *Nat. Commun.* 9, 743.
- Yuan, J., Zhang, Y., Zhou, L., Zhang, G., Yip, H.-L., Lau, T.-K., Lu, X., Zhu, C., Peng, H., and Johnson, P.A. (2019). Single-junction organic solar cell with over 15% efficiency using fused-ring acceptor with electron-deficient core. *Joule* 3, 1140–1151.
- Zhang, Q., Kan, B., Liu, F., Long, G., Wan, X., Chen, X., Zuo, Y., Ni, W., Zhang, H., Li, M., et al. (2015). Small-molecule solar cells with efficiency over 9%. *Nat. Photonics* 9, 35–41.
- Cui, Y., Yao, H., Zhang, J., Zhang, T., Wang, Y., Hong, L., Xian, K., Xu, B., Zhang, S., Peng, J., et al. (2019). Over 16% efficiency organic photovoltaic cells enabled by a chlorinated acceptor with increased open-circuit voltages. *Nat. Commun.* 10, 2515.
- Wang, J., Zheng, Z., Zhang, D., Zhang, J., Zhou, J., Liu, J., Xie, S., Zhao, Y., Zhang, Y., Wei, Z., et al. (2019). Regulating bulk-heterojunction molecular orientations through surface free energy control of hole-transporting layers for high-performance organic solar cells. *Adv. Mater.* 31, e1806921.
- Li, W., Roelofs, W.S., Turbiez, M., Wienk, M.M., and Janssen, R.A. (2014). Polymer solar cells with diketopyrrolopyrrole conjugated polymers as the electron donor and electron acceptor. *Adv. Mater.* 26, 3304–3309.
- Pan, F., Sun, C., Li, Y., Tang, D., Zou, Y., Li, X., Bai, S., Wei, X., Lv, M., Chen, X., Li, Y., et al. (2019). Solution-processable n-doped graphene-containing cathode interfacial materials for high-performance organic solar cells. *Energy Environ. Sci.* 12, 3400–3411.
- Lin, Y., Adilbekova, B., Firdaus, Y., Yengel, E., Faber, H., Sajjad, M., Zheng, X., Yarali, E., Seikhani, A., Bakr, O.M., et al. (2019). 17% Efficient organic solar cells based on liquid exfoliated WS₂ as a replacement for PEDOT:PSS. *Adv. Mater.* 31, e1902965.
- Sun, R., Guo, J., Wu, Q., Zhang, Z., Yang, W., Guo, J., Shi, M., Zhang, Y., Kahmann, S., Ye, L., et al. (2019). A multi-objective optimization-based layer-by-layer blade-coating approach for organic solar cells: rational control of vertical stratification for high performance. *Energy Environ. Sci.* 12, 3118–3132.
- Zhang, J., Tan, H.S., Guo, X., Facchetti, A., and Yan, H. (2018). Material insights and challenges for non-fullerene organic solar cells based on small molecular acceptors. *Nat. Energy* 3, 720–731.
- Yang, J., Xiao, B., Tang, A., Li, J., Wang, X., and Zhou, E. (2019). Aromatic-diimide-based n-type conjugated polymers for all-polymer solar cell applications. *Adv. Mater.* 31, e1804699.
- Zhao, X., and Zhan, X. (2011). Electron transporting semiconducting polymers in organic electronics. *Chem. Soc. Rev.* 40, 3728–3743.
- Zhou, E., Cong, J., Wei, Q., Tajima, K., Yang, C., and Hashimoto, K. (2011). All-polymer solar cells from perylene diimide based copolymers: material design and phase separation control. *Angew. Chem. Int. Ed. Engl.* 50, 2799–2803.
- Choi, J., Kim, W., Kim, S., Kim, T.-S., and Kim, B.J. (2019). Influence of acceptor type and polymer molecular weight on the mechanical properties of polymer solar cells. *Chem. Mater.* 31, 9057–9069.
- Wang, G., Melkonyan, F.S., Facchetti, A., and Marks, T.N. (2019). All-polymer solar cells: recent progress, challenges, and prospects. *Angew. Chem. Int. Ed. Engl.* 58, 4129–4142.
- Kim, T., Kim, J.H., Kang, T.E., Lee, C., Kang, H., Shin, M., Wang, C., Ma, B., Jeong, U., Kim, T.S., and Kim, B.J. (2015). Flexible, highly efficient all-polymer solar cells. *Nat. Commun.* 6, 8547.
- Zhou, N., Lin, H., Lou, S.J., Yu, X., Guo, P., Manley, E.F., Loser, S., Hartnett, P., Huang, H., Wasielewski, M.R., et al. (2014). Morphology-performance relationships in high-efficiency all-polymer solar cells. *Adv. Energy Mater.* 4, 1300785.
- Xu, Y., Yuan, J., Zhou, S., Seifrid, M., Ying, L., Li, B., Huang, F., Bazan, G.C., and Ma, W. (2019). Ambient processable and stable all-polymer organic solar cells. *Adv. Funct. Mater.* 29, 1806747.
- Zhu, L., Zhong, W., Qiu, C., Lyu, B., Zhou, Z., Zhang, M., Song, J., Xu, J., Wang, J., Ali, J., et al. (2019). Aggregation-induced multilength scaled morphology enabling 11.76% efficiency in all-polymer solar cells using printing fabrication. *Adv. Mater. Weinheim* 31, e1902899.
- Li, Z., Ying, L., Zhu, P., Zhong, W., Li, N., Liu, F., Huang, F., and Cao, Y. (2019). A generic green solvent concept boosting the power conversion efficiency of all-polymer solar cells to 11%. *Energy Environ. Sci.* 12, 157–163.
- Zhan, X., Tan, Z., Domercq, B., An, Z., Zhang, X., Barlow, S., Li, Y., Zhu, D., Kippelen, B., and Marder, S.R. (2007). A high-mobility electron-transport polymer with broad absorption and its use in field-effect transistors and all-polymer solar cells. *J. Am. Chem. Soc.* 129, 7246–7247.
- Kozma, E., Kotowski, D., Bertini, F., Luzzati, S., and Catellani, M. (2010). Synthesis of donor-acceptor poly(perylenediimide-altoligothiophene) copolymers as n-type materials for polymeric solar cells. *Polymer* 51, 2264–2270.
- Zhou, Y., Kurosawa, T., Ma, W., Guo, Y., Fang, L., Vandewal, K., Diao, Y., Wang, C., Yan, Q., Reinspach, J., et al. (2014). High performance all-polymer solar cell via polymer side-chain engineering. *Adv. Mater.* 26, 3767–3772.
- Sun, H., Tang, Y., Koh, C.W., Ling, S., Wang, R., Yang, K., Yu, J., Shi, Y., Wang, Y., Woo, H.Y., et al. (2019). High-performance all-polymer solar cells enabled by an n-type polymer based on a fluorinated imide-functionalized arene. *Adv. Mater. Weinheim* 31, e1807220.
- Moore, J.R., Albert-Seifried, S., Rao, A., Massip, S., Watts, B., Morgan, D.J., Friend, R.H., McNeill, C.R., and Sirringhaus, H. (2011). Polymer blend solar cells based on a high-mobility naphthalenediimide-based polymer acceptor: device physics, photophysics and morphology. *Adv. Energy Mater.* 1, 230–240.
- Liu, X., Huettner, S., Rong, Z., Sommer, M., and Friend, R.H. (2012). Solvent additive control of morphology and crystallization in semiconducting polymer blends. *Adv. Mater.* 24, 669–674.
- Cheng, P., Ye, L., Zhao, X., Hou, J., Li, Y., and Zhan, X. (2014). Binary additives synergistically boost the efficiency of all-polymer solar cells up to 3.45%. *Energy Environ. Sci.* 7, 1351–1356.
- Oh, J., Kranthiraja, K., Lee, C., Gunasekar, K., Kim, S., Ma, B., Kim, B.J., and Jin, S.H. (2016). Side-chain fluorination: an effective approach to achieving high-performance all-polymer solar cells with efficiency exceeding 7%. *Adv. Mater.* 28, 10016–10023.
- Li, Z., Xu, X., Zhang, W., Meng, X., Genene, Z., Ma, W., Mammo, W., Yartsev, A., Andersson, M.R., Janssen, R.A.J., and Wang, E. (2017). 9.0% power conversion efficiency from ternary all-polymer solar cells. *Energy Environ. Sci.* 10, 2212–2221.
- Halls, J.J., Walsh, C.A., Greenham, N.C., Marseglia, E.A., Friend, R.H., Moratti, S.C., and Holmes, A.B. (1995). Efficient photodiodes form interpenetrating polymer networks. *Nature* 376, 498–500.
- Yu, G., and Heeger, A.J. (1995). Charge separation and photovoltaic conversion in polymer composites with internal donor/acceptor heterojunctions. *J. Appl. Phys.* 78, 4510–4515.

38. Liu, M., Yang, J., Yin, Y., Zhang, Y., Zhou, E., Guo, F., and Zhao, L. (2018). Novel perylene diimide-based polymers with electron-deficient segments as the comonomer for efficient all-polymer solar cells. *J. Mater. Chem. A* 6, 414–422.
39. Jung, J., Lee, W., Lee, C., Ahn, H., and Kim, B.J. (2016). Controlling molecular orientation of naphthalenediimide-based polymer acceptors for high performance all-polymer solar cells. *Adv. Energy Mater.* 6, 1600504.
40. Mori, D., Bente, H., Okada, I., Ohkita, H., and Ito, S. (2014). Low-bandgap donor/acceptor polymer blend solar cells with efficiency exceeding 4%. *Adv. Energy Mater.* 4, 1301006.
41. Mu, C., Liu, P., Ma, W., Jiang, K., Zhao, J., Zhang, K., Chen, Z., Wei, Z., Yi, Y., Wang, J., et al. (2014). High-efficiency all-polymer solar cells based on a pair of crystalline low-bandgap polymers. *Adv. Mater.* 26, 7224–7230.
42. Yao, H., Bai, F., Hu, H., Arunagiri, L., Zhang, J., Chen, Y., Yu, H., Chen, S., Liu, T., Lai, J.Y.L., et al. (2019). Efficient all-polymer solar cells based on a new polymer acceptor achieving 10.3% power conversion efficiency. *ACS Energy Lett.* 4, 417–422.
43. Zhang, Z.G., Yang, Y., Yao, J., Xue, L., Chen, S., Li, X., Morrison, W., Yang, C., and Li, Y. (2017). Constructing a strongly absorbing low-bandgap polymer acceptor for high-performance all-polymer solar cells. *Angew. Chem. Int. Ed. Engl.* 56, 13503–13507.
44. Li, Y., Meng, H., Liu, T., Xiao, Y., Tang, Z., Pang, B., Li, Y., Xiang, Y., Zhang, G., Lu, X., et al. (2019). 8.78% Efficient all-polymer solar cells enabled by polymer acceptors based on a B←N embedded electron-deficient unit. *Adv. Mater.* 31, e1904585.
45. Zhao, R., Lin, B., Feng, J., Dou, C., Ding, Z., Ma, W., Liu, J., and Wang, L. (2019). Amorphous polymer acceptor containing B←N units matches various polymer donors for all-polymer solar cells. *Macromolecules* 52, 7081–7088.
46. Long, X., Ding, Z., Dou, C., Zhang, J., Liu, J., and Wang, L. (2016). Polymer acceptor based on double B←N bridged bipyridine (BNBP) unit for high-efficiency all-polymer solar cells. *Adv. Mater.* 28, 6504–6508.
47. Hwang, Y.J., Earmme, T., Courtright, B.A., Eberle, F.N., and Jenekhe, S.A. (2015). N-type semiconducting naphthalene diimide-perylene diimide copolymers: controlling crystallinity, blend morphology, and compatibility toward high-performance all-polymer solar cells. *J. Am. Chem. Soc.* 137, 4424–4434.
48. Wu, J., Meng, Y., Guo, X., Zhu, L., Liu, F., and Zhang, M. (2019). All-polymer solar cells based on a novel narrow-bandgap polymer acceptor with power conversion efficiency over 10%. *J. Mater. Chem. A* 7, 16190–16196.
49. Fabiano, S., Chen, Z., Vahedi, S., Facchetti, A., Pignataro, B., and Loi, M.A. (2011). Role of photoactive layer morphology in high fill factor all-polymer bulk heterojunction solar cells. *J. Mater. Chem.* 21, 5891.
50. Mori, D., Bente, H., Okada, I., Ohkita, H., and Ito, S. (2014). Highly efficient charge-carrier generation and collection in polymer/polymer blend solar cells with a power conversion efficiency of 5.7%. *Energy Environ. Sci.* 7, 2939–2943.
51. Fan, B., Ying, L., Zhu, P., Pan, F., Liu, F., Chen, J., Huang, F., and Cao, Y. (2017). All-polymer solar cells based on a conjugated polymer containing siloxane-functionalized side chains with efficiency over 10%. *Adv. Mater.* 29, 1703906.
52. Deshmukh, K.D., Qin, T., Gallaher, J.K., Liu, A.C.Y., Gann, E., O'Donnell, K., Thomsen, L., Hodgkiss, J.M., Watkins, S.E., and McNeill, C.R. (2015). Performance, morphology and photophysics of high open-circuit voltage, low band gap all-polymer solar cells. *Energy Environ. Sci.* 8, 332–342.
53. Kietzke, T., Hörhold, H.-H., and Neher, D. (2005). Efficient polymer solar cells based on M3EH-PPV. *Chem. Mater.* 17, 6532–6537.
54. Schubert, M., Dolfin, D., Frisch, J., Roland, S., Steyrlauthner, R., Stiller, B., Chen, Z., Scherf, U., Koch, N., Facchetti, A., and Neher, D. (2012). Influence of aggregation on the performance of all-polymer solar cells containing low-bandgap naphthalenediimide copolymers. *Adv. Energy Mater.* 2, 369–380.
55. Zhou, E., Cong, J., Hashimoto, K., and Tajima, K. (2013). Control of miscibility and aggregation via the material design and coating process for high-performance polymer blend solar cells. *Adv. Mater. Weinheim* 25, 6991–6996.
56. Earmme, T., Hwang, Y.J., Murari, N.M., Subramaniam, S., and Jenekhe, S.A. (2013). All-polymer solar cells with 3.3% efficiency based on naphthalene diimide-selenophene copolymer acceptor. *J. Am. Chem. Soc.* 135, 14960–14963.
57. Zhang, C., Heumuel, T., Gruber, W., Almora, O., Du, X., Ying, L., Chen, J., Unruh, T., Cao, Y., Li, N., and Brabec, C.J. (2019). Comprehensive investigation and analysis of bulk-heterojunction microstructure of high-performance PCE11:PCBM solar cells. *ACS Appl. Mater. Interfaces* 11, 18555–18563.
58. Ye, L., Li, S., Liu, X., Zhang, S., Ghasemi, M., Xiong, Y., Hou, J., and Ade, H. (2018). Quenching to the percolation threshold in organic solar cells. *Joule* 3, 443–458.
59. Wadsworth, A., Hamid, Z., Bidwell, M., Ashraf, R.S., Khan, J.I., Anjum, D.H., Cendra, C., Yan, J., Rezasoltani, E., Guilbert, A.A.Y., et al. (2018). Progress in poly (3-hexylthiophene) organic solar cells and the influence of its molecular weight on device performance. *Adv. Energy Mater.* 8, 1801001.
60. Zhou, N., Dudnik, A.S., Li, T.I., Manley, E.F., Aldrich, T.J., Guo, P., Liao, H.C., Chen, Z., Chen, L.X., Chang, R.P., et al. (2016). All-polymer solar cell performance optimized via systematic molecular weight tuning of both donor and acceptor polymers. *J. Am. Chem. Soc.* 138, 1240–1251.
61. Kang, H., Lee, W., Oh, J., Kim, T., Lee, C., and Kim, B.J. (2016). From fullerene-Polymer to All-polymer solar cells: the importance of molecular packing, orientation, and morphology control. *Acc. Chem. Res.* 49, 2424–2434.
62. Kang, H., Uddin, M.A., Lee, C., Kim, K.H., Nguyen, T.L., Lee, W., Li, Y., Wang, C., Woo, H.Y., and Kim, B.J. (2015). Determining the role of polymer molecular weight for high-performance all-polymer solar cells: its effect on polymer aggregation and phase separation. *J. Am. Chem. Soc.* 137, 2359–2365.
63. Deshmukh, K.D., Matsidik, R., Prasad, S.K.K., Connal, L.A., Liu, A.C.Y., Gann, E., Thomsen, L., Hodgkiss, J.M., Sommer, M., and McNeill, C.R. (2018). Tuning the molecular weight of the electron accepting polymer in all-polymer solar cells: impact on morphology and charge generation. *Adv. Funct. Mater.* 28, 1707185.
64. Zhang, M., Guo, X., Ma, W., Ade, H., and Hou, J. (2015). A large-bandgap conjugated polymer for versatile photovoltaic applications with high performance. *Adv. Mater.* 27, 4655–4660.
65. Vezie, M.S., Few, S., Meager, I., Pieridou, G., Döring, B., Ashraf, R.S., Goñi, A.R., Bronstein, H., McCulloch, I., Hayes, S.C., et al. (2016). Exploring the origin of high optical absorption in conjugated polymers. *Nat. Mater.* 15, 746–753.
66. Shi, S., Chen, P., Chen, Y., Feng, K., Liu, B., Chen, J., Liao, Q., Tu, B., Luo, J., Su, M., et al. (2019). A narrow-bandgap n-type polymer semiconductor enabling efficient all-polymer solar cells. *Adv. Mater.* 31, e1905161.
67. Yuan, J., Zhang, Y., Zhou, L., Zhang, C., Lau, T.K., Zhang, G., Lu, X., Yip, H.L., So, S.K., Beaupré, S., et al. (2019). Fused benzothiadiazole: a building block for n-type organic acceptor to achieve high-performance organic solar cells. *Adv. Mater.* 31, e1807577.
68. Yu, R., Yao, H., Chen, Z., Xin, J., Hong, L., Xu, Y., Zu, Y., Ma, W., and Hou, J. (2019). Enhanced π - π interactions of nonfullerene acceptors by volatilizable solid additives in efficient polymer solar cells. *Adv. Mater.* 31, e1900477.
69. Min, J., Luponosov, Y.N., Gasparini, N., Richter, M., Bakirov, A.V., Shcherbina, M.A., Chvalun, S.N., Grodd, L., Grigorian, S., Ameri, T., et al. (2015). Effects of alkyl terminal chains on morphology, charge generation, transport, and recombination mechanisms in solution-processed small molecule bulk heterojunction solar cells. *Adv. Energy Mater.* 5, 1500386.
70. Wang, T., Sun, R., Xu, S., Guo, J., Wang, W., Guo, J., Jiao, X., Wang, J., Jia, S., Zhu, X., et al. (2019). A wide-bandgap D-A copolymer donor based on a chlorine substituted acceptor unit for high performance polymer solar cells. *J. Mater. Chem. A* 7, 14070–14078.
71. Li, W., Hendriks, K.H., Furlan, A., Wienk, M.M., and Janssen, R.A. (2015). High quantum efficiencies in polymer solar cells at energy losses below 0.6 eV. *J. Am. Chem. Soc.* 137, 2231–2234.
72. Veldman, D., Meskers, S.C.J., and Janssen, R.A.J. (2009). The energy of charge-transfer states in electron donor-acceptor blends: insight into the energy losses in organic solar cells. *Adv. Funct. Mater.* 19, 1939–1948.
73. Wang, W., Sun, R., Guo, J., Guo, J., and Min, J. (2019). An oligothiophene-fullerene molecule with a balanced donor-acceptor backbone for high-performance single-component organic solar cells. *Angew. Chem. Int. Ed. Engl.* 58, 14556–14561.

74. Kawashima, K., Tamai, Y., Ohkita, H., Osaka, I., and Takimiya, K. (2015). High-efficiency polymer solar cells with small photon energy loss. *Nat. Commun.* **6**, 10085.
75. Wang, M., Wang, H., Yokoyama, T., Liu, X., Huang, Y., Zhang, Y., Nguyen, T.Q., Aramaki, S., and Bazan, G.C. (2014). High open circuit voltage in regioregular narrow band gap polymer solar cells. *J. Am. Chem. Soc.* **136**, 12576–12579.
76. Wang, Y., Qian, D., Cui, Y., Zhang, H., Hou, J., Vandewal, K., Kirchartz, T., and Gao, F. (2018). Optical gaps of organic solar cells as a reference for comparing voltage losses. *Adv. Energy Mater.* **8**, 1801352.
77. Qian, D., Zheng, Z., Yao, H., Tress, W., Hopper, T.R., Chen, S., Li, S., Liu, J., Chen, S., Zhang, J., et al. (2018). Design rules for minimizing voltage losses in high-efficiency organic solar cells. *Nat. Mater.* **17**, 703–709.
78. Yao, J., Kirchartz, T., Vezie, M.S., Faist, M.A., Gong, W., He, Z., Wu, H., Troughton, J., Watson, T., Bryant, D., and Nelson, J. (2015). Quantifying losses in open-circuit voltage in solution-processable solar cells. *Phys. Rev. Applied* **4**, 014020.
79. Eisner, F.D., Azzouzi, M., Fei, Z., Hou, X., Anthopoulos, T.D., Dennis, T.J.S., Heeney, M., and Nelson, J. (2019). Hybridization of local exciton and charge-transfer states reduces nonradiative voltage losses in organic solar cells. *J. Am. Chem. Soc.* **141**, 6362–6374.
80. Han, Y.W., Jeon, S.J., Lee, H.S., Park, H., Kim, K.S., Lee, H.W., and Moon, D.K. (2019). Evaporation-free nonfullerene flexible organic solar cell modules manufactured by an all-solution process. *Adv. Energy Mater.* **9**, 1902065.
81. Rivnay, J., Noriega, R., Kline, R.J., Salleo, A., and Toney, M.F. (2011). Quantitative analysis of lattice disorder and crystallite size in organic semiconductor thin films. *Phys. Rev. B* **84**, 045203.